Separation of bulk and surface contributions to the damping of permalloy on large-area chemical-vapor-deposited MoS_2

Henry De Libero,[1] Evelyn Chalmers,[2] Noel Natera-Cordero,[2] Andrew Strudwick,[2] Ivan J. Vera-Marun,[3] and Thomas Thomson[1,*]

[1] *Department of Computer Science, The University of Manchester, Manchester, M13 9PL, United Kingdom*

[2] *Graphene Engineering and Innovation Centre, The Masdar Building, The University of Manchester, Manchester, M1 3BB, United Kingdom*

[3] *Department of Physics and Astronomy, The University of Manchester, Manchester, M13 9PL, United Kingdom*

(Received 11 July 2025; revised 25 October 2025; accepted 22 January 2026; published 4 March 2026)

The ability to develop practical spintronic devices that use 2D van der Waals materials requires research on wafer-scale materials typically fabricated using chemical vapor deposition (CVD). In this report, we investigate spin pumping effects using ferromagnetic resonance spectroscopy (FMR) in wafer-scale transition-metal dichalcogenide–ferromagnetic (FM) heterostructures, specifically, MoS_2-$Ni_{0.8}Fe_{0.2}$ bilayers with varying $Ni_{0.8}Fe_{0.2}$ thicknesses. The FMR measurements allow the phenomenological damping parameter α of the FM layer to be determined, with increased values often attributed to injection of spins across an interface through spin pumping. Our results on sputtered $Ni_{0.8}Fe_{0.2}(t)$ films deposited on monolayer and bilayer CVD-grown MoS_2 show a lower contribution to α from surface effects than a film of the same thickness deposited on SiO_2. A reduction in surface damping is often attributed to a drop in spin pumping, but this work demonstrates that other interfacial effects such as spin-memory loss must also be considered in determining the physical origin of the measured damping parameter.

DOI: 10.1103/wfsl-4mhb

I. INTRODUCTION

The potential of two-dimensional (2D) van der Waals materials in spintronics has generated considerable interest in recent years [1]. Monolayer graphene has been shown to be an effective medium for spin transport [2], given its low spin-orbit coupling (SOC) [3], long spin-diffusion lengths [4], and high carrier mobility [5]. More recently, the use of one-dimensional ferromagnetic contacts has shown efficient spin injection into encapsulated graphene, demonstrating the progress of graphene spintronic devices [6]. Unlike spin transport, spin-charge interconversion requires materials with a high SOC [7], and transition-metal dichalcogenides (TMDs) are promising material candidates that provide this functionality. Two of the most well-studied TMDs, molybdenum disulfide (MoS_2) and tungsten disulfide (WS_2), have been shown to exhibit large spin-to-charge interconversion, mostly attributed to the interfacial Rashba-Edelstein effect [8–10]. More recently, it has been shown that TMDs (such as tungsten ditelluride WTe_2) can produce spin-orbit torques (SOTs) capable of achieving field-free switching in a perpendicularly magnetized ferromagnet (FM) in intimate contact, a key requirement for SOT magnetic random access memory (SOT-MRAM) [11–13]; however, there currently exists no method for fabricating these TMDs that is compatible with wafer-scale fabrication. Large-area growth by chemical vapor deposition (CVD) has been achieved for the previously mentioned MoS_2 and WS_2 [14,15], making them clear choices for further study of TMD-FM bilayers for SOT applications.

To investigate materials for SOT-MRAM, the phenomenological damping parameter α is often studied, which can be measured using ferromagnetic resonance (FMR) spectroscopy [16]. A high damping parameter indicates a fast relaxation of the magnetization due to substantial energy dissipation. A system with a low damping parameter has a slowly relaxing magnetization with low energy dissipation. Therefore, magnetic switching can be optimized through the creation of devices that are critically damped [17]. Damping is also often correlated with spin-pumping processes and spin charge interconversion in FM-normal metal bilayers. For example, large spin-to-charge conversion via the inverse Rashba-Edelstein effect was observed to be correlated with an enhancement

*Contact author: thomas.thomson@manchester.ac.uk

Published by the American Physical Society under the terms of the Creative Commons Attribution 4.0 International license. Further distribution of this work must maintain attribution to the author(s) and the published article's title, journal citation, and DOI.

to the damping in TMD-permalloy ($Ni_{0.8}Fe_{0.2}$) bilayers [9]. An increase in damping due to spin pumping in MoS_2-$Ni_{0.8}Fe_{0.2}$ was attributed to extrinsic spin-orbit coupling in the MoS_2 [18]; however, it has also been shown that $MoSe_2$-CoFeB with atomically clean interfaces has no enhancement in damping, suggesting that extrinsic defects may be the main contributor to the apparent increase in damping, rather than spin pumping [19]. Therefore, a clear understanding of the contributions to the damping parameter from the interface and the bulk is required for optimizing TMD-FM heterostructures for SOT applications.

In this work, we report on a study to separate bulk and surface contributions to the damping parameter in large-area monolayer and bilayer MoS_2-permalloy heterostructures, where the monolayer and bilayer MoS_2 has been grown by CVD. By separating out the bulk and surface contributions to the damping parameter in the FM layer, we can determine if enhancements to the damping parameter are due to changes in the FM layer or from surface effects such as spin pumping or spin-memory loss [20].

II. EXPERIMENTAL METHODS

Large-area growth of MoS_2 was achieved using a metal-organic CVD reactor in the vertical showerhead configuration. MoS_2 was grown on 50-mm-diameter Si-SiO_2(290 nm) substrates. The substrate was treated with O_2 plasma prior to growth. The pressure of the reactor chamber was set at 25 mbar, and the growth time was 22 min. The substrate was heated to 600 °C, while no heating was applied to the showerhead. $Mo(CO)_6$ and di-tert butyl sulfide (DTBS) were used as precursors, with N_2 as the carrier gas. The N_2 flow rate for $Mo(CO)_6$ and DTBS was 35 and 350 sccm, respectively. The flow rate of H_2 used throughout was 10 sccm.

After growth of MoS_2, Raman [21] spectroscopy was used to confirm the quality of the as-grown MoS_2 at three locations: the center of the wafer, the edge, and the midpoint between them. In Raman spectroscopy, incident laser light excites the unique vibrational modes of the MoS_2 lattice, so detection of the corresponding shift in frequency represents the energy absorbed due to this excitation and can be used to detect the presence of monolayer MoS_2. Using this, uniform monolayer MoS_2 was detected within 5×5-mm^2 areas along the edges of the 50-mm-diameter wafer.

The edges of the 50-mm-diameter wafer were scribed into five 5×5-mm^2 samples, which were then transferred to a separate dc magnetron sputtering system (AJA International ATC 2200-V), where a series of thicknesses of $Ni_{0.8}Fe_{0.2}$ was deposited. A control series of samples was deposited directly on Si-SiO_2 (290 nm) under the same conditions. For all depositions, the base pressure of the chamber was 3×10^{-8} Torr, and the working pressure of the argon gas was 3×10^{-3} Torr. The sputtering plasma power was set at 50 W to avoid damaging the MoS_2 from high-energy bombardment. The samples were then capped with 4 nm of MgO to protect the permalloy.

A Rigaku SmartLab diffractometer was used to perform x-ray reflectometry (XRR) and x-ray diffraction (XRD) measurements. The XRR data were fitted using a Fresnel model and a Parratt recursive algorithm [22] in the GENX software package [23], providing values for the thickness, density, and roughness of individual layers. The XRD measurements were performed in the grazing-incidence (GI) configuration, where the angle of incidence was fixed at 0.5° and the 2θ detector angle was swept. The use of GI-XRD reduces the diffraction intensity from the substrate, allowing the detection of peaks from the thin film that would otherwise be obscured by the strong substrate signal. The static magnetic properties were measured using vibrating-sample magnetometry (VSM) using a Microsense Model 10 vibrating-sample magnetometer.

The FMR measurements were undertaken using a purpose-designed vector network analyzer (VNA)-based spectrometer (VNA-FMR) consisting of an Agilent model N5224A VNA [24] and a NanOsc coplanar waveguide (CPW) placed in a field produced by a GMW 5403 electromagnet. The VNA supplied a frequency-swept signal from 10 MHz to 43 GHz. The coplanar waveguide converted this rf signal into an in-plane oscillating Oersted field to drive the precession of the sample magnetization. Samples were placed film-side down on the CPW. The CPW was positioned in the deep gap field of an electromagnet supplying a dc magnetic field. Resonant precession leads to a drop in transmitted power through the CPW, measured by the VNA as scattering parameters S_{12} and S_{21} (the ratio of the power measured at ports 1 and 2) [25,26]. Figure 1(a) shows a schematic of the sample on the CPW during FMR. Figure 1(b) shows an example of the data. A full two-port short-open-load-through calibration was performed on the VNA prior to the measurement to correct for any losses and reflections due to the cables and connectors. The nonmagnetic, frequency-dependent contributions (from the CPW and substrate) that dominate the frequency-swept signal are subtracted from the measured spectrum. To remove any possible magnetic-field-dependent properties from the CPW (from contamination, for example), the full frequency spectrum of just the CPW is also subtracted. This procedure removes most of the nonmagnetic background contribution, but as can be seen in Fig. 1(b) from the horizontal lines, a small residual contribution remains; however, this does not materially impact the subsequent analysis.

The measured spectra are then parametrized by fitting the frequency-dependent S_{12} to a sum of a symmetric and antisymmetric Lorentzian functions, representing the real and imaginary parts of the dynamics [27], allowing for the extraction of resonant frequency and linewidth. To determine the dynamic magnetic properties of samples,

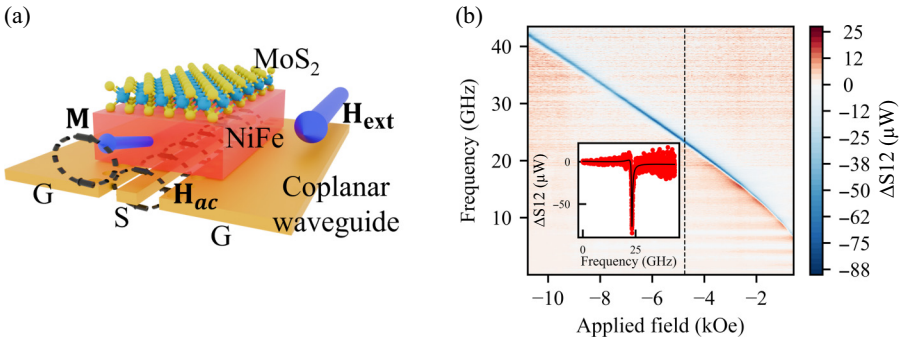


FIG. 1. (a) Illustration of FMR in a MoS_2-NiFe bilayer. The sample is placed flip-chip on a coplanar waveguide (CPW). The sample is magnetized in the plane by a static applied field, $\mathbf{H}_{ext}$. An rf signal is supplied by a VNA to the CPW, which generates an oscillating in-plane Oersted field ($\mathbf{H}_{ac}$) that drives the magnetization $\mathbf{M}$ of the sample to precess. The precessing magnetization then generates a spin current perpendicular to both $\mathbf{H}_{ac}$ and $\mathbf{H}_{ext}$. The change in power transmitted through the waveguide is measured by the VNA. (b) FMR spectrum of an MoS_2-NiFe(7.4 nm)-MgO sample as a function of frequency and applied field. Inset: ΔS_{12} frequency-swept data for $H_{ext} = -4.75$ kOe, where its position on the spectrum is indicated by the dotted line. The solid black line indicates a complex Lorentzian fit to the data, from which the resonant frequency and linewidth are extracted.

a specific solution for the Landau-Lifshitz-Gilbert (LLG) [16,28] equation was used. Assuming a thin film with no strong in-plane uniaxial anisotropy (as is appropriate for permalloy thin films) in a uniform in-plane applied field, the solution to the LLG is given by the Kittel equation [26],

$$f_r = \frac{\gamma}{2\pi}\sqrt{H_{ext}(H_{ext} + 4\pi M_{eff})}, \tag{1}$$

where f_r is the resonant frequency, H_{ext} is the applied field, M_{eff} is the effective magnetization, and $\gamma = ge/2m_e$, in which g is the spectroscopic g factor, and e and m_e are the electron charge and mass, respectively. In the LLG equation, the phenomenological damping parameter α is then determined using the linear relation of resonant linewidth Δf_r to applied field, given by [29]

$$\Delta f_r = \Delta f_0 + \gamma\alpha(2H_{ext} + 4\pi M_{eff}), \tag{2}$$

where Δf_0 is the inhomogeneous linewidth-broadening term.

Although α is given by a single parameter in the LLG equation, it has many different contributions, which for the purposes of this work can be broadly separated into surface and bulk effects [29,30]. The surface contribution to the damping can be increased by spin pumping, as the pure spin current generated by a precessing magnetization transfers angular momentum into a spin-orbit-coupled layer in intimate contact [31]. The nature of the interface plays a key role in the transfer of spin from the FM layer to the high SOC coupling layer; for example, damping can be enhanced through two-magnon scattering (TMS) [32]. Spin-memory loss (SML) can also contribute to the damping parameter, especially in bilayers with a high SOC layer [33]. In SML, spins propagating across an interface (e.g., via spin pumping) will scatter at the interface, dissipating spin angular momentum and increasing the damping. Bulk damping contributions are typically dependent on the lattice of the FM layer, where the transfer of energy through spin dissipation to the surrounding lattice results in increased damping. To disentangle surface and bulk effects, the thickness of the permalloy layer was varied, as the damping parameter varies with FM layer thickness t_{FM} as [30]

$$\alpha_{eff} = \alpha_B + \alpha_S\frac{1}{t_{FM}}, \tag{3}$$

where α_S and α_B are the surface and bulk contributions to the damping parameter, respectively.

III. STRUCTURAL RESULTS

Table I shows the thicknesses and roughnesses obtained from XRR for MoS_2-$Ni_{0.8}Fe_{0.2}$-MgO samples and a control series of SiO_2-$Ni_{0.8}Fe_{0.2}$-MgO. The thickness of the permalloy layer increases linearly with deposition time,

TABLE I. XRR-determined thickness (t) and roughness (σ) values for SiO_2 control and MoS_2 samples with different NiFe deposition times.

Deposition time (s)	Underlayer	t_{NiFe} (nm)	σ_{NiFe} (nm)	t_{MoS_2} (nm)	σ_{MoS_2} (nm)
300	MoS_2	4.7	0.9	0.7	0.4
	SiO_2	5.1	0.9	–	–
325	MoS_2	5.2	1.1	0.8	0.7
	SiO_2	5.4	1.1	–	–
350	MoS_2	6.2	1.0	0.8	0.4
	SiO_2	5.9	1.2	–	–
400	MoS_2	7.4	1.0	0.9	0.3
	SiO_2	6.8	1.0	–	–
500	MoS_2	8.7	1.2	0.4	0.3
	SiO_2	8.1	1.1	–	–

as expected. Note that a nonmagnetic seed layer to provide adhesion to the substrate was not used, as a seed layer such as tantalum could contribute to the damping signal by providing a sink for any spin current generated. To achieve a fit to the XRR data with physically reasonable parameters for the SiO_2-$Ni_{0.8}Fe_{0.2}$-MgO samples, an initial growth layer of <1 nm of $Ni_{0.8}Fe_{0.2}$ was required at the SiO_2-$Ni_{0.8}Fe_{0.2}$ interface. This was done following prior work, where it has been suggested that the growth of the first few atomic planes should be included in the model as a separate layer [27,34]. There was no significant change in the growth rate of permalloy on MoS_2 when compared to SiO_2. Attempts were also made to fit the MoS_2 samples to a model without an MoS_2 layer. This confirmed the presence of MoS_2, as models excluding an MoS_2 layer were not able to reproduce the measured XRR data for any physically reasonable set of parameters. Furthermore, the interfacial roughness parameters in Table I (σ_{NiFe} and σ_{MoS_2}) are consistently lower for NiFe on MoS_2 than on SiO_2. The low roughness values indicate a pristine and undamaged interface between the NiFe and MoS_2. The mean fitted thickness of the MoS_2 layer was 0.7 ± 0.2 nm, suggesting the presence of monolayer MoS_2; however, interfacial roughness parameters (σ_{MoS_2}) are of the same order of magnitude as the MoS_2 thickness, which could indicate the presence of bilayers as well as monolayers over a large area.

Raman spectroscopy was used to confirm the presence of MoS_2 after sputtering. Figure 2 shows an example Raman spectrum of MoS_2 after sputtering of permalloy. The E^1_{2g} and A_{1g} peaks are detected, and they are separated by a spatial frequency of approximately 20 cm^{-1}. This demonstrates the structural integrity of the MoS_2 layer after deposition of the permalloy. The E^1_{2g} and A_{1g} peak separation is consistent with the presence of either one or two MoS_2 layers [21]. The presence of bilayers is possible,

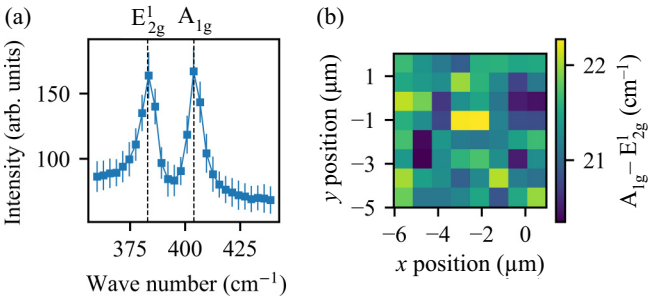


FIG. 2. Raman data for MoS_2-$Ni_{0.8}Fe_{0.2}$(6.2 nm)-MgO. (a) Average of all spectra from a 7×7-μm^2 scan area. Vertical dashed lines indicate the E^{2g}_1 and A_{1g} modes. Error bars represent the standard deviation of the shift value across all map locations. (b) Heat map of the $A_{1g} - E^{2g}_1$ separation. The scan was taken in 1-μm steps.

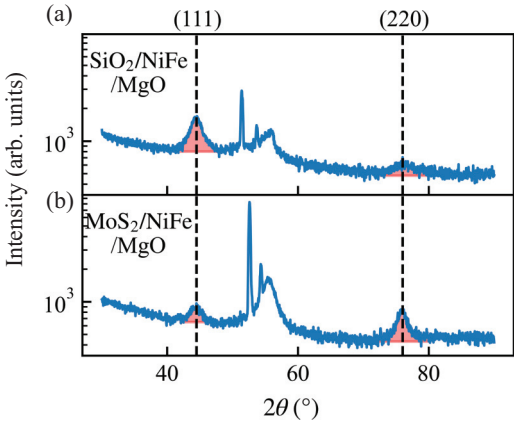


FIG. 3. Grazing-incidence x-ray diffraction spectra for (a) SiO_2-$Ni_{0.8}Fe_{0.2}$-MgO and (b) SiO_2-MoS_2-$Ni_{0.8}Fe_{0.2}$-MgO. Vertical dashed lines indicate the permalloy powder diffraction peaks for the (111) and (220) crystal planes. Red highlighted regions indicate the area under the NiFe crystal peaks. Note that peaks around 50°–60° correspond to the Si substrate.

given that large-area growth often results in islands of multiple layers forming. This can be seen in Fig. 2(b), where hot spots of bi- or trilayers are present within a 7×7-μm^2 area.

Figure 3 shows the GI-XRD spectra for permalloy on SiO_2 and MoS_2. Figure 3(a) demonstrates that permalloy predominately grows along the (111) crystal plane on SiO_2, though a small (220) peak can be seen. To measure the relative intensities of these peaks, a Gaussian with a second-order polynomial background was fitted to each peak. The area of the fitted Gaussian with background subtracted gives relative areas of 88% for (111) at 44° and 12% for (220) at 76° for NiFe on SiO_2; however, as shown in Fig. 3(b), permalloy on MoS_2 has a more dominant (220) peak, with a relative peak area of 60% compared to the (111) peak on MoS_2 (40%). This therefore indicates a more mixed crystallographic phase for permalloy grown on MoS_2, due to the permalloy being grown on a crystalline layer (MoS_2), rather than on an amorphous substrate (SiO_2).

IV. MAGNETIC RESULTS AND DISCUSSION

Figure 4 shows the in-plane and out-of-plane (OOP) hysteresis loops of MoS_2-NiFe-MgO and SiO_2-NiFe-MgO. The magnetization was calculated from measuring the raw magnetic moment and normalizing by the volume of the sample, where the thickness used was the thickness of the NiFe layer obtained from XRR. The initial few atomic layers of NiFe are excluded from the NiFe thickness, treating them as magnetically dead layers. The value of M_S is fractionally increased on MoS_2 compared to SiO_2: $M_S^{MoS_2} = 794 \pm 16$ emu/cm^3 and $M_S^{SiO_2} = 760 \pm 14$ emu/cm^3, where the superscript MoS_2 or SiO_2 denotes

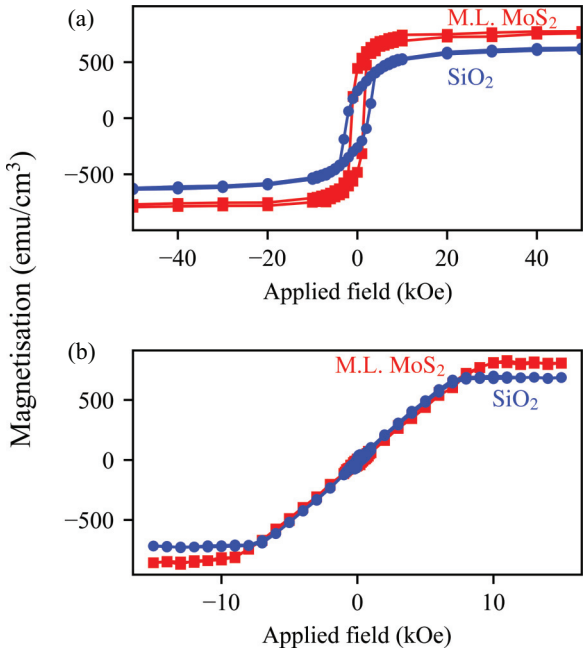


FIG. 4. Hysteresis loops for SiO_2-NiFe(5.1 nm)-MgO (blue) and MoS_2(0.8 nm)-NiFe(4.7 nm)-MgO (red), from VSM. (a) In-plane hysteresis loops, enlarged to ±50 Oe. (b) Out-of-plane hysteresis.

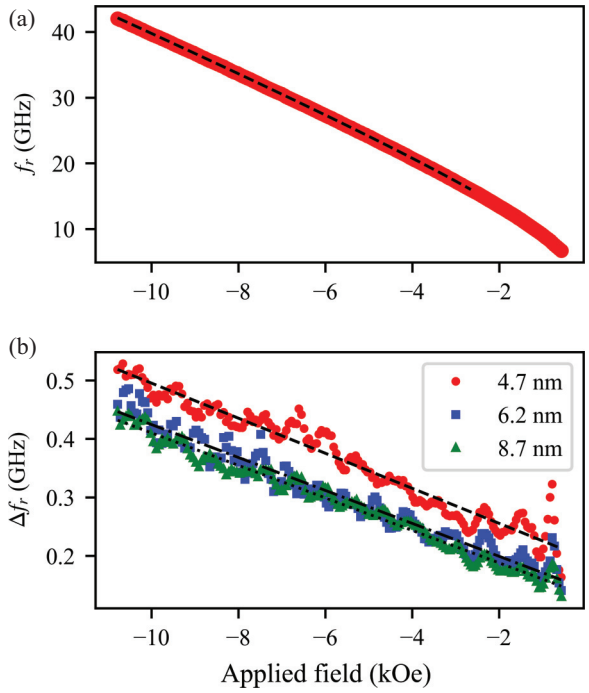


FIG. 5. Resonant-frequency and linewidth dependence on in-plane applied field for MoS_2-NiFe(t)-MgO. (a) Resonant frequency versus applied field for MoS_2-NiFe(8.7 nm)-MgO. The dashed black line shows a fit to the data using Eq. (1). (b) Resonant-frequency linewidth versus applied field for MoS_2-NiFe(t)-MgO, where t is the thickness of the NiFe in nanometers (see legend). The dotted and dashed black lines show fits to Eq. (2).

the presence or absence of the TMD layer. The uncertainty in M_S quoted here is dominated by the uncertainty in the XRR-determined thickness values for NiFe.

In the OOP configuration, it is harder to saturate the sample with MoS_2, requiring a saturating field H_S of approximately 8 kOe for SiO_2 compared to approximately 11 kOe for MoS_2. The saturation field can be used to calculate the measured anisotropy energy density, $K_{meas} \approx K_1 + K_d + 2K_{surf}/t$, where K_1, K_d, and K_{surf} are the magnetocrystalline, shape, and surface anisotropy terms, respectively. For thin films, the shape anisotropy (given by $K_d = 2\pi M_S^2$) is typically the dominant anisotropy term in K_{meas}. Using this, $K_d^{MoS_2} = 4.0 \pm 0.2 \times 10^6$ erg/cm^3 and $K_d^{SiO_2} = 3.6 \pm 0.1 \times 10^6$ erg/cm^3. The total measured anisotropy K_{meas} can also be approximated as $K_{meas} \approx (1/2)H_S M_S$, and in a system with no additional anisotropy terms (e.g., magnetocrystalline or surface), this should be equal to K_d. This is true for the MoS_2-NiFe sample, with $K_{eff}^{MoS_2} = 3.97 \pm 0.08 \times 10^6$ erg/cm^3; however, $K_{eff}^{SiO_2} = 3.04 \pm 0.06 \times 10^6$ erg/cm^3, suggesting that there is an additional anisotropy term that is reducing the energy cost for the NiFe to become saturated OOP.

The VNA-FMR spectroscopy results are shown in Fig. 5. Figure 5(a) shows the FMR for MoS_2-NiFe (8.7 nm)-MgO with a fit to Eq. (1), agreeing well over a wide frequency range. The linewidth data and fit to Eq. (2) for different NiFe thicknesses are shown in Fig. 5(b). Note that small oscillations in the linewidth are likely artefacts from residual background contributions as described in Sec. II. The relationship between t_{FM} and α can be seen immediately, as a thicker FM layer results in a reduced linewidth and therefore a smaller α. It should also be noted that despite using in-plane FMR, no significant TMS was observed, as shown by the linearity of Δf_R with H_r over a wide frequency range (10–40 GHz), since TMS is expected to result in a severe nonlinearity linewidth with frequency [35,36]. This linear agreement can also be seen in the linewidth of SiO_2-NiFe-MgO (see Fig. 6). OOP FMR measurements also showed a higher damping for SiO_2-NiFe-MgO (see Figs. 6 and 7). Therefore, we conclude that TMS is not the origin of the observed differences in damping.

Figure 8(a) shows the thickness dependence of α for permalloy with and without the MoS_2 SOC layer. Using Eq. (3), the surface and damping contributions to the damping parameter are determined. The surface damping α_S of permalloy on MoS_2 is almost half that of on SiO_2, where $\alpha_S^{MoS_2} = 0.011 \pm 0.002$ nm and $\alpha_S^{SiO_2} = 0.023 \pm 0.005$ nm. α_S is large when spin-flip scattering associated with spin pumping is present [29,30]. The reduction in α_S would therefore suggest almost no

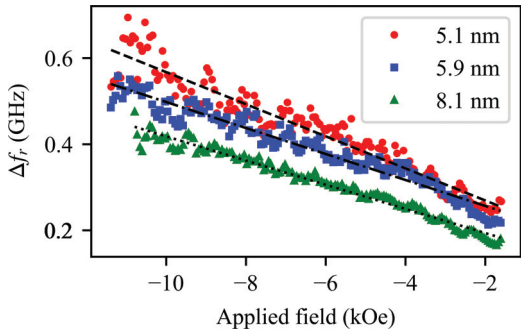


FIG. 6. Resonant-frequency linewidth Δf_r against in-plane applied field for SiO_2-NiFe(t)-MgO, where t is the thickness of the NiFe layer in nanometers (see legend). Dotted and dashed black lines indicate fits to Eq. (2).

spin pumping from permalloy into MoS_2, similar to observations of atomically smooth interfaces, as seen in the case of $MoSe_2$-CoFeB [19]; however, spin pumping into SiO_2 is unlikely, so the claim that spin pumping is reduced for an FM on MoS_2 is incomplete. To better understand the interface, one has to consider other surface phenomena such as SML [33]. SML occurs when spins are scattered at the interface due to surface roughness, defects [37], and orbital hybridization [38], resulting in an enhancement to the surface damping. In the case of MoS_2, it has been predicted that induced strain in monolayer MoS_2 increases spin relaxation [39]. This is opposite to what we observe here, as spin relaxation is predominantly in the permalloy layer. The reduction in surface damping contributions shown here could therefore indicate a low spin-memory loss between permalloy and MoS_2, due to a good lattice match between NiFe and MoS_2, compared to the amorphous SiO_2. This is consistent with theoretical predictions regarding the extent of SML in FM-HM multilayers, where spin scattering (and thus SML) at an interface is increased by lattice mismatch [37].

The amount of disorder at the interface can also be inferred from the inhomogeneous linewidth Δf_0 in Eq. (2).

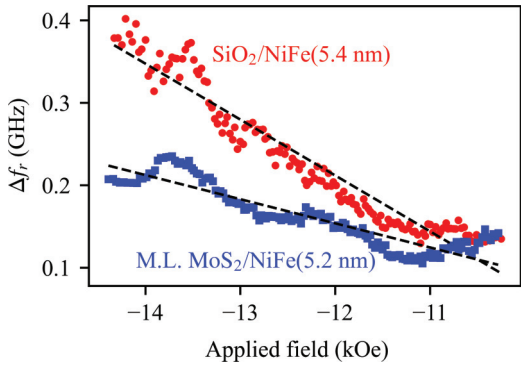


FIG. 7. FMR resonant-frequency linewidth Δf_r against out-of-plane applied field.

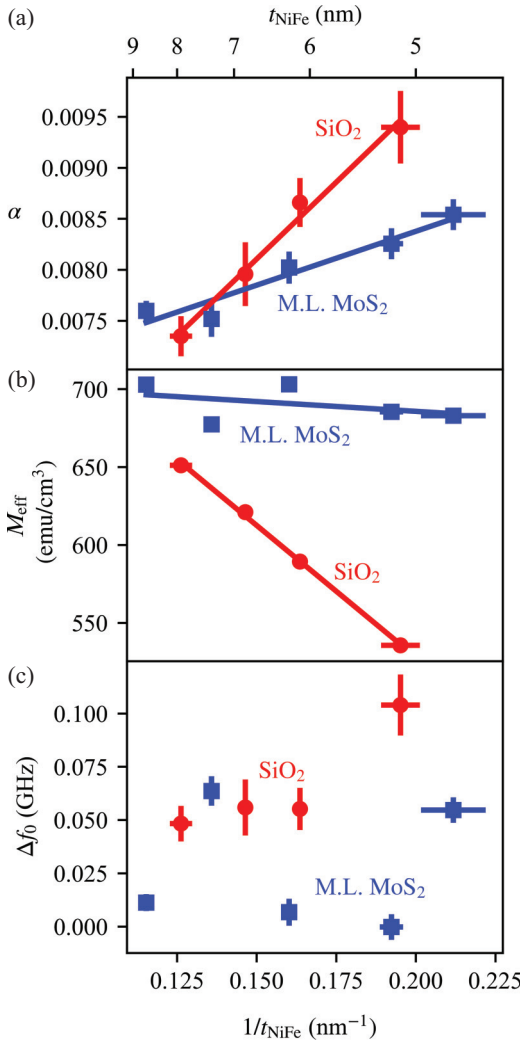


FIG. 8. Dynamic magnetic parameters versus NiFe thickness. (a) Phenomenological damping parameter α. (b) Effective magnetization M_{eff}. (c) Inhomogeneous broadening Δf_0. Labels on plots indicate the underlayer used. Solid lines show fits to the data using Eq. (3) for (a) and Eq. (4) for (b).

The values of Δf_0 for SiO_2-NiFe and MoS_2-NiFe are shown in Fig. 8(c). Aside from a single outlier, Δf_0 for SiO_2-NiFe is consistently higher than MoS_2-NiFe. The inhomogeneous linewidth broadening originates from local variations in magnetization and anisotropy across the sample [40]. Magnetic inhomogeneity can also be directly related to the interfacial disorder of thin films [41]; hence, an increase in interfacial disorder is consistent with higher values of Δf_0. Therefore, the higher values of Δf_0 for SiO_2-NiFe support the conclusion that the larger surface-damping contribution for SiO_2-NiFe arises from interfacial spin-flip scattering due to structural inhomogeneity at the interface.

SML is not only driven by disorder but also scales with the SOC of the adjacent layer [37]. If SOC were the dominant contribution to SML, it should be larger in

MoS_2-NiFe than in SiO_2-NiFe due to the negligibly small SOC of SiO_2 compared to MoS_2; however, we observe a greater surface contribution to the damping and a higher Δf_0 for SiO_2-NiFe. This implies that the dominant contribution to SML in SiO_2-NiFe is interfacial disorder, which is reduced in MoS_2-NiFe.

We also note that a similar study has been conducted using graphene (Gr) interlayers on NiFe-Cu and NiFe-Gr-Cu [42]. There, it was shown that the damping enhancement seen in NiFe-Cu was suppressed by the insertion of a Gr interlayer [42]. This suppression is attributed to a reduced spin flow out of the NiFe due to the high contact resistance at the Gr-Cu interface. Given the insulating nature of SiO_2, spin pumping from NiFe at the SiO_2-NiFe interface should be smaller than in MoS_2-NiFe, and thus the damping of MoS_2-NiFe should be higher; however, the lower damping observed here in MoS_2-NiFe is not consistent with this interpretation. Therefore, measurement of damping alone is not sufficient for understanding the nature of spin backflow in these systems. We suggest complementary studies such as measurements of the inverse spin-Hall effect [43], which could help provide greater insight into spin pumping and 2D materials [44].

To further examine the surface phenomena in MoS_2-$Ni_{0.8}Fe_{0.2}$ bilayers, the thickness dependence of M_{eff} determined from FMR measurements was studied. The effective magnetization is related to bulk saturation magnetization M_S by

$$M_{\text{eff}} = M_S - \frac{K_{\text{surf}}}{2\pi M_S t_{\text{FM}}}, \tag{4}$$

where K_{surf} is the surface anisotropy energy density and t_{FM} is the thickness of the ferromagnetic layer [18]. Figure 8(b) shows the thickness dependence of M_{eff}. Here, K_{surf} can be estimated, with $K_{\text{surf}}^{SiO_2} = 1.03$ ergs/cm^2 and $K_{\text{surf}}^{MoS_2} = 0.15$ ergs/cm^2, showing that the surface anisotropy of permalloy on MoS_2 is nearly an order of magnitude lower. An increase in K_{surf} corresponds to a thin film with greater OOP anisotropy and hence a lower K_{eff}. This is consistent with the VSM results, where $K_{\text{eff}}^{SiO_2}$ is lower than $K_{\text{eff}}^{MoS_2}$, and this could be an indication of a change in strain, which can increase the OOP anisotropy.

To understand the magnetic behavior of the whole heterostructure, the bulk contribution to damping was also extracted using Eq. (3). From the data in Fig. 8(a), the bulk damping of permalloy was measured at $\alpha_B^{SiO_2} = 0.0046 \pm 0.0004$ on SiO_2 and $\alpha_B^{MoS_2} = 0.0063 \pm 0.0003$ on MoS_2. The physical origin of bulk damping is spin-lattice scattering within the ferromagnetic layer [29]. This would be consistent with the XRD results (see Fig. 3), as the mixed crystallographic phase is likely to imply a different grain-boundary structure, which would increase the amount of spin-lattice scattering in the permalloy when sputtered onto MoS_2.

V. SUMMARY AND CONCLUSIONS

We have explored the physical origin of changes to the damping parameter in MoS_2-$Ni_{0.8}Fe_{0.2}$ bilayers. By separating out the surface and bulk contributions to the damping parameter, we find that bulk damping contributions in permalloy (e.g., spin-lattice scattering) are increased when sputtered onto CVD-grown MoS_2. This is attributed to the change in crystallographic ordering, where NiFe on MoS_2 has approximately equal amounts of (111) and (220) ordering, leading to more effective spin scattering compared with NiFe on SiO_2, which is predominantly (111) ordered. Conversely, surface contributions (e.g., interfacial spin-flip scattering, spin pumping) decrease for permalloy on MoS_2. Since spin pumping into SiO_2 is unlikely, other interfacial phenomena such as spin-memory loss are the more likely explanation for the increased surface-damping contribution. The reduction in K_{surf} is consistent with the reduction in α_S due to a drop in spin-memory loss, indicating that sputtered permalloy onto MoS_2 has an interface with low disorder and low atomic hybridization. This work highlights the importance of determining the physical origins of enhanced damping in spin pumping measurements, as enhanced effective damping can also arise from spin-lattice scattering. While increases in surface damping are often attributed to spin pumping, these results suggest that other interfacial effects, such as spin-memory loss, should also be considered.

ACKNOWLEDGMENTS

The support of The University of Manchester Graphene NOWNANO program and the EPSRC "International Network for Spintronics: From Material Development to Novel Energy Efficient Technologies," project reference EP/V007211/1, is gratefully acknowledged. I.J.V.-M. acknowledges the Horizon Europe Project "2D Heterostructure Non-volatile Spin Memory Technology" (2DSPIN-TECH) and is supported by UKRI Grant No. 10101734 (The University of Manchester).

DATA AVAILABILITY

The data that support the findings of this article are openly available [45]; embargo periods may apply.

[1] E. C. Ahn, 2D materials for spintronic devices, npj 2D Materials and Applications **4**, 1 (2020).

[2] A. Avsar, H. Ochoa, F. Guinea, B. Özyilmaz, B. J. van Wees, and I. J. Vera-Marun, Colloquium: Spintronics in graphene and other two-dimensional materials, Rev. Mod. Phys. **92**, 021003 (2020).

[3] A. H. Castro Neto, F. Guinea, N. M. R. Peres, K. S. Novoselov, and A. K. Geim, The electronic properties of graphene, Rev. Mod. Phys. **81**, 109 (2009).

[4] W. Han and R. K. Kawakami, Spin relaxation in single-layer and bilayer graphene, Phys. Rev. Lett. **107**, 047207 (2011).

[5] K. S. Novoselov, A. K. Geim, S. V. Morozov, D. Jiang, Y. Zhang, S. V. Dubonos, I. V. Grigorieva, and A. A. Firsov, Electric field effect in atomically thin carbon films, Science **306**, 666 (2004).

[6] D. Burrow, J. C. Toscano-Figueroa, V. H. Guarochico-Moreira, K. Omari, I. V. Grigorieva, T. Thomson, and I. J. Vera-Marun, Spin polarised quantised transport via one-dimensional nanowire-graphene contacts, Commun. Mater. **6**, 33 (2025).

[7] L. Liu, C.-F. Pai, Y. Li, H. W. Tseng, D. C. Ralph, and R. A. Buhrman, Spin-torque switching with the giant spin Hall effect of tantalum, Science **336**, 555 (2012).

[8] J. Mendes, A. Aparecido-Ferreira, J. Holanda, A. Azevedo, and S. Rezende, Efficient spin to charge current conversion in the 2D semiconductor MoS_2 by spin pumping from yttrium iron garnet, Appl. Phys. Lett. **112**, 242407 (2018).

[9] H. Bangar, A. Kumar, N. Chowdhury, R. Mudgal, P. Gupta, R. S. Yadav, S. Das, and P. K. Muduli, Large spin-to-charge conversion at the two-dimensional interface of transition-metal dichalcogenides and permalloy, ACS Appl. Mater. Interfaces **14**, 41598 (2022).

[10] T. S. Ghiasi, A. A. Kaverzin, P. J. Blah, and B. J. van Wees, Charge-to-spin conversion by the Rashba–Edelstein effect in two-dimensional van der Waals heterostructures up to room temperature, Nano Lett. **19**, 5959 (2019).

[11] L. Liu, C. Zhou, X. Shu, C. Li, T. Zhao, W. Lin, J. Deng, Q. Xie, S. Chen, J. Zhou, R. Guo, H. Wang, J. Yu, S. Shi, P. Yang, S. Pennycook, A. Manchon, and J. Chen, Symmetry-dependent field-free switching of perpendicular magnetization, Nat. Nanotechnol. **16**, 277 (2021).

[12] I.-H. Kao, R. Muzzio, H. Zhang, M. Zhu, J. Gobbo, S. Yuan, D. Weber, R. Rao, J. Li, J. H. Edgar, J. E. Goldberger, J. Yan, D. G. Mandrus, J. Hwang, R. Cheng, J. Katoch, and S. Singh, Deterministic switching of a perpendicularly polarized magnet using unconventional spin–orbit torques in WTe_2, Nat. Mater. **21**, 1029 (2022).

[13] Y. Luo, Q. Chen, R. Li, Y. Wang, W. Lv, B. Zhang, Y. Fan, H. Wu, and Z. Zeng, Enhanced spin–orbit torque and field-free switching in Au/TMDs/Ni hybrid structures, Nanoscale **15**, 3142 (2023).

[14] Y.-H. Lee, X.-Q. Zhang, W. Zhang, M.-T. Chang, C.-T. Lin, K.-D. Chang, Y.-C. Yu, J. T.-W. Wang, C.-S. Chang, L.-J. Li, and T.-W. Lin, Synthesis of large-area MoS_2 atomic layers with chemical vapor deposition, Adv. Mater. **24**, 2320 (2012).

[15] R. I. Romanov, M. G. Kozodaev, D. I. Myakota, A. G. Chernikova, S. M. Novikov, V. S. Volkov, A. S. Slavich, S. S. Zarubin, P. S. Chizhov, R. R. Khakimov, A. A. Chouprik, C. S. Hwang, and A. M. Markeev, Synthesis of large area two-dimensional MoS_2 films by sulfurization of atomic layer deposited MoO_3 thin film for nanoelectronic applications, ACS Appl. Nano Mater. **2**, 7521 (2019).

[16] T. Gilbert, A phenomenological theory of damping in ferromagnetic materials, IEEE Trans. Magn. **40**, 3443 (2004).

[17] I. Tudosa, J. A. Katine, S. Mangin, and E. E. Fullerton, Perpendicular spin-torque switching with a synthetic antiferromagnetic reference layer, Appl. Phys. Lett. **96**, 212504 (2010).

[18] R. Bansal, A. Kumar, N. Chowdhury, N. Sisodia, A. Barvat, A. Dogra, P. Pal, and P. K. Muduli, Extrinsic spin-orbit coupling induced enhanced spin pumping in few-layer MoS_2/Py, J. Magn. Magn. Mater. **476**, 337 (2019).

[19] B. Lu, Y. Niu, Q. Chen, P. K. J. Wong, Q. Guo, W. Jiang, A. Rath, S. J. Pennycook, L. Wang, K. Xia, Y. Zhai, A. T. Shen Wee, and W. Zhang, Is semiconducting transition-metal dichalcogenide suitable for spin pumping? Nano Lett. **25**, 35 (2025).

[20] J.-C. Rojas-Sánchez, N. Reyren, P. Laczkowski, W. Savero, J.-P. Attané, C. Deranlot, M. Jamet, J.-M. George, L. Vila, and H. Jaffrès, Spin pumping and inverse spin Hall effect in platinum: The essential role of spin-memory loss at metallic interfaces, Phys. Rev. Lett. **112**, 106602 (2014).

[21] C. Lee, H. Yan, L. E. Brus, T. F. Heinz, J. Hone, and S. Ryu, Anomalous lattice vibrations of single- and few-layer MoS_2, ACS Nano **4**, 2695 (2010).

[22] L. G. Parratt, Surface studies of solids by total reflection of x-rays, Phys. Rev. **95**, 359 (1954).

[23] A. Glavic and M. Björck, *GenX 3*: The latest generation of an established tool, J. Appl. Crystallogr. **55**, 1063 (2022).

[24] N. A. B. Johansson, *Interlayer Exchange Coupling in* Co/Pd-NiFe *Films Studied by Vector Network Analyser Ferromagnetic Resonance*, Ph.D. thesis, The University of Manchester (2018).

[25] I. S. Maksymov and M. Kostylev, Broadband stripline ferromagnetic resonance spectroscopy of ferromagnetic films, multilayers and nanostructures, Physica E: Low-Dimensional Systems Nanostructures **69**, 253 (2015).

[26] C. Kittel, On the theory of ferromagnetic resonance absorption, Phys. Rev. **73**, 155 (1948).

[27] H. Waring, *Magnetisation Dynamics in Multilayer Spintronic Materials*, Ph.D. thesis, University of Manchester (2022).

[28] L. Landau and E. Lifshitz, in *Perspectives in Theoretical Physics*, edited by L. Pitaevski (Pergamon, Amsterdam, 1992), p. 51.

[29] Y. Zhao, Q. Song, S.-H. Yang, T. Su, W. Yuan, S. S. P. Parkin, J. Shi, and W. Han, Experimental investigation of temperature-dependent Gilbert damping in permalloy thin films, Sci. Rep. **6**, 22890 (2016).

[30] E. Barati, M. Cinal, D. M. Edwards, and A. Umerski, Gilbert damping in magnetic layered systems, Phys. Rev. B **90**, 014420 (2014).

[31] Y. Tserkovnyak, A. Brataas, and Gerrit E. W. Bauer, Spin pumping and magnetization dynamics in metallic multilayers, Phys. Rev. B **66**, 224403 (2002).

[32] S. Yoshii, K. Kato, E. Shigematsu, R. Ohshima, Y. Ando, K. Usami, and M. Shiraishi, Significant suppression of two-magnon scattering in ultrathin Co by controlling the surface magnetic anisotropy at the Co/nonmagnet interfaces, Phys. Rev. B **106**, 174414 (2022).

[33] T. Silva, E. R. J. Edwards, H. T. Nembach, O. Karis, M. Weiler, and A. J. Berger, in *Spintronics XI*, Vol. 10732, edited by H.-J. Drouhin, J.-E. Wegrowe, M. Razeghi, and H. Jaffrès, International Society for Optics and Photonics (SPIE, San Diego, California, United States, 2018), 1073206.

[34] H. J. Waring, Y. Li, N. A. B. Johansson, C. Moutafis, I. J. Vera-Marun, and T. Thomson, Exchange stiffness constant

determination using multiple-mode FMR perpendicular standing spin waves, J. Appl. Phys. **133**, 063901 (2023).

[35] A. G. A. G. Gurevich and G. A. G. A. Melkov, *Magnetization Oscillations and Waves* (CRC Press, Boca Raton, FL, 1996).

[36] M. Körner, K. Lenz, R. A. Gallardo, M. Fritzsche, A. Mücklich, S. Facsko, J. Lindner, P. Landeros, and J. Fassbender, Two-magnon scattering in permalloy thin films due to rippled substrates, Phys. Rev. B **88**, 054405 (2013).

[37] K. Gupta, Rien J. H. Wesselink, R. Liu, Z. Yuan, and P. J. Kelly, Disorder dependence of interface spin memory loss, Phys. Rev. Lett. **124**, 087702 (2020).

[38] M. Lim and H.-W. Lee, Spin-memory loss induced by bulk spin–orbit coupling at ferromagnet/heavy-metal interfaces, Appl. Phys. Lett. **118**, 042408 (2021).

[39] H. Ochoa, F. Guinea, and V. I. Fal'ko, Spin memory and spin-lattice relaxation in two-dimensional hexagonal crystals, Phys. Rev. B **88**, 195417 (2013).

[40] L. Jin, H. Zhang, X. Tang, F. Bai, and Z. Zhong, Effects of ruthenium seed layer on the microstructure and spin dynamics of thin permalloy films, J. Appl. Phys. **113**, 053902 (2013).

[41] J. M. Shaw, H. T. Nembach, and T. J. Silva, Roughness induced magnetic inhomogeneity in Co/Ni multilayers: Ferromagnetic resonance and switching properties in nanostructures, J. Appl. Phys. **108**, 093922 (2010).

[42] W. Gannett, M. W. Keller, H. T. Nembach, T. J. Silva, and A. N. Chiaramonti, Suppression of spin pumping between $Ni_{80}Fe_{20}$ and Cu by a graphene interlayer, J. Appl. Phys. **117**, 213907 (2015).

[43] E. Saitoh, M. Ueda, H. Miyajima, and G. Tatara, Conversion of spin current into charge current at room temperature: Inverse spin-Hall effect, Appl. Phys. Lett. **88**, 182509 (2006), publisher: American Institute of Physics.

[44] Z. Tang, E. Shikoh, H. Ago, K. Kawahara, Y. Ando, T. Shinjo, and M. Shiraishi, Dynamically generated pure spin current in single-layer graphene, Phys. Rev. B **87**, 140401(R) (2013).

[45] H. De Libero, E. Chalmers, N. Natera-Cordero, A. Strudwick, I. J. Vera-Marun, and T. Thomson, Separation of bulk and surface contributions to the damping of permalloy on large-area CVD MoS_2, https://doi.org/10.5281/zenodo.18391896 (2026).